

Accurate Modeling of LEGO-like vdW Heterostructures: Integrating Machine Learned with Anisotropic Interlayer Potentials

Hekai Bu,^{1,*} Wenwu Jiang,^{1,*} Penghua Ying,^{2,†} Ting Liang,³ Zheyong Fan,⁴ and Wengen Ouyang^{1,5,‡}

¹*Department of Engineering Mechanics, School of Civil Engineering,
Wuhan University, Wuhan, Hubei 430072, China*

²*Department of Physical Chemistry, School of Chemistry, Tel Aviv University, Tel Aviv, 6997801, Israel*

³*Department of Electronic Engineering and Materials Science and Technology Research Center,
The Chinese University of Hong Kong, Shatin, N.T., Hong Kong SAR, 999077, China*

⁴*College of Physical Science and Technology, Bohai University, Jinzhou 121013, China*

⁵*State Key Laboratory of Water Resources Engineering and Management,
Wuhan University, Wuhan, Hubei 430072, China*

(Dated: April 18, 2025)

Accurately modeling the structural reconstruction and thermodynamic behavior of van der Waals (vdW) heterostructures remains a significant challenge due to the limitations of conventional force fields in capturing their complex mechanical, thermal, electronic, and tribological properties. To address these limitations, we develop a hybrid framework that combines single-layer machine-learned potential (sMLP) with physics-based anisotropic interlayer potential (ILP), effectively decoupling intralayer and interlayer interactions. This sMLP+ILP approach modularizes the modeling of vdW heterostructures like assembling LEGOs, reducing the required training configurations by at least an order of magnitude compared to the pure MLP approach, while retaining predictive accuracy and computational efficiency. We validate our framework by accurately reproducing the mechanical properties of graphite, and resolving intricate Moiré patterns in graphene/*h*-BN bilayers and graphene/graphene/*h*-BN trilayer heterostructures, achieving excellent agreement with experimental observations. Leveraging the developed sMLP+ILP approach, we reveal the stacking order-dependent formation of Moiré superlattice in trilayer graphene/*h*-BN/MoS₂ heterostructures, demonstrating its ability to accurately model large-scale vdW systems comprising hundreds of thousands of atoms with near *ab initio* precision. These findings demonstrate that hybrid sMLP+ILP framework remarkably outperforms existing pure machine-learned or empirical potentials, offering a scalable and transferable solution for accurately and extensively modeling complex vdW materials across diverse applications, including sliding ferroelectricity, thermal management, resistive switching, and superlubric nanodevices.

I. INTRODUCTION

Van der Waals (vdW) heterojunctions, formed by vertically stacking two-dimensional (2D) layered materials, exhibit unique mechanical [1, 2], thermal transport [3–7], electronic [8–13], and tribological [14–20] properties. Accurate modeling of their structural reconstruction and thermodynamic behaviors at the atomic scale is crucial for understanding these properties. However, theoretical investigation at this scale presents a non-trivial challenge, as heterostructure superlattices typically contain hundreds of thousands of atoms due to intrinsic lattice mismatches between monolayers (e.g., $\sim 1.8\%$ between hexagonal boron nitride (*h*-BN) and graphene (Gr)), making them computationally intractable for first-principles approaches such as density functional theory (DFT).

Due to the anisotropic nature of vdW layered materials, atomic interactions in layered materials can be divided into intralayer interactions, which involve strong

covalent bonding, and weak vdW interlayer interactions, which include short-range electronic repulsion, long-range attractive dispersion and electrostatic interactions. Building on these physical insights, various empirical potentials, such as the reactive empirical bond order (REBO) potential [21, 22], the Tersoff potential [23, 24], and the Stillinger–Weber (SW) potential [25, 26] combined with Lennard-Jones (LJ) terms, have been developed over the past two decades [27, 28] to model both homogeneous and heterogeneous layered materials. However, the two-body LJ terms predict an overly shallow sliding potential energy surface (PES) [29–31], as they fail to capture the anisotropic nature of vdW layered materials. To address this limitation, registry-dependent interlayer potential (ILP) approaches [30, 32] have been proposed, incorporating not only on the interatomic distance (as in LJ) but also on interatomic relative lateral displacement to accurately describe the overlap of electronic cloud overlap, i.e., the origin of short-range interlayer repulsion. To better capture the long-range interactions, further improvements [33–39] incorporate the long-range dispersion term from the Tkatchenko–Scheffler correction scheme [40] along with the electrostatic interaction term. To date, ILP approaches have been widely used to model the structural reconstruction [10, 41, 42], mechanical properties, [2, 43–45] nanotribological prop-

* These authors contributed equally to this work.

† hityingph@tauex.tau.ac.il

‡ w.g.ouyang@whu.edu.cn

erties [16, 36, 46–48], thermal transport [49–51], and growth behaviors [52, 53] of layered materials and other vdW heterostructures [44, 54–58], aligning well with experimental observations.

Although ILP approaches have significantly advanced the modeling of vdW heterostructures, they are typically combined with empirical potentials to describe intralayer covalent bonding, leading to following two main limitations: (i) the existing empirical potential models are primarily parameterized for pristine periodic crystal structures, making them less transferable to the systems with structural defects such as edges, vacancies, and grain boundaries [59], or to new 2D allotropes [60]; (ii) the accuracy of empirical potentials often falls short of the level of first-principles calculations. To overcome these limitations, one may resort to the emerging machine-learned potential (MLP) approach [61, 62]. Instead of distinguishing the intralayer and interlayer interactions based on physical insights, MLPs learn directly from *ab initio* data, mapping the atomic positions into corresponding site energies and their gradients (atomic forces) using invariant [63–67] or equivariant [68–71] feature representations for the atomic environments. Dedicated MLPs for 2D monolayers and bilayers can achieve high accuracy in describing short-range interactions [72–75], which effectively captures the sliding PES or structural reconstruction.

However, most MLPs impose an effective cutoff of several angstroms to reduce computational costs, making them insufficient for capturing London dispersion interactions that extend over several nanometers [42, 76]. Several efforts have been proposed to address this limitation, including incorporating LJ-like corrections [77, 78] or DFT-D3 dispersion [76] corrections. Additionally, the graph neural network potential (GNNP) based on message-passing architectures offers a promising solution by allowing interlayer interactions to be propagated along the atomic graph through multiple convolutional layers. However, current GNNPs are highly computationally demanding and remain impractical for modeling large heterostructures with tens of thousands of atoms [73]. Another limitation of MLP approaches is their reliance on sufficiently large reference datasets to accurately represent local atomic environments. Capturing interlayer interactions using these MLP approaches becomes particularly challenging for complex heterostructures containing three or more distinct layers. A comprehensive MLP for such systems must account for various stacking orders, surface and interface conditions, and bulk properties—along with different interlayer distances and sliding PES across various temperatures and pressures for each configuration. This complexity may explain why existing MLPs for vdW heterostructures are limited to bilayer systems, with no models yet developed for heterostructures containing three or more distinct component layers.

In the present study, we propose a LEGO-like hybrid framework that combines single-layer MLP (*sMLP*) and physics-based ILP using different cutoffs, effectively

decoupling short-range intralayer and long-range interlayer interactions (see Figure 1(a)). The advantages are twofold: *sMLP* with more parameters reduces the required reference dataset by focusing on single layers while improving accuracy and applicability compared to empirical potentials, while ILP with fewer parameters ensures efficiency despite using a large cutoff. This approach enables the construction of potential models for vdW heterostructures like assembling LEGOs, eliminating the need for extensive reference datasets to capture complex chemical environments, including stacking orders, surface and interface boundary conditions, interlayer spacings, and corresponding sliding PES. Here, we chose the highly efficient neuroevolution potential (NEP) framework [67, 79, 80] to train the *sMLP* models for monolayer 2D materials, such as Gr, *h*-BN and molybdenum disulfide (MoS₂). Note that this workflow is readily adaptable to other MLP frameworks for broader applications. By training *sMLP* and ILP models separately on a small dataset of state-of-the-art DFT calculations, we demonstrate that this hybrid framework achieves *ab initio* accuracy while maintaining computational efficiency comparable to existing empirical potentials. Furthermore, we validate its transferability by applying it to bilayer and trilayer complex vdW heterostructures, investigating their mechanical properties and structural reconstruction accompanied by complex Moiré patterns. We implement our *sMLP*+ILP framework into open-source molecular dynamics (MD) packages, including LAMMPS [81] and GPUMD [82]. Notably, an exceptional computational speed exceeding 2×10^6 atom · step/s is achieved in GPUMD using a single NVIDIA RTX 4090 consumer desktop GPU for Gr/MoS₂/*h*-BN heterostructures comprising 423,552 atoms, enabling sub-micron scale simulations of complex 2D vdW heterostructures at near *ab initio* accuracy for the first time.

II. RESULTS AND DISCUSSION

A. Model Definition

In our hybrid *sMLP*+ILP approach, the total potential energy $V_{\text{tot}}^{\text{sMLP+ILP}}$ for a configuration with N atoms and M layers is computed as:

$$V_{\text{tot}}^{\text{sMLP+ILP}} = \sum_{k=1}^M \sum_{l=1}^M [V_{kl}^{\text{sMLP}} \delta_{kl} + V_{kl}^{\text{ILP}} (1 - \delta_{kl})], \quad (1)$$

where V_{kl}^{sMLP} and V_{kl}^{ILP} represent the potential energy of the *sMLP* model and the ILP model of the k^{th} layer within neighbors in the l^{th} layer, respectively. δ_{kl} is the Kronecker delta function.

For these two site potential terms, we construct two independent neighbor lists for atom i : Ω_i^{sMLP} and Ω_i^{ILP} . The intralayer neighbors j ($j \in \Omega_i^{\text{sMLP}}$) are searched within the same layer as atom i using a cutoff of $R_{\text{cut}}^{\text{sMLP}}$, while the interlayer neighbors k ($k \in \Omega_i^{\text{ILP}}$) are identified

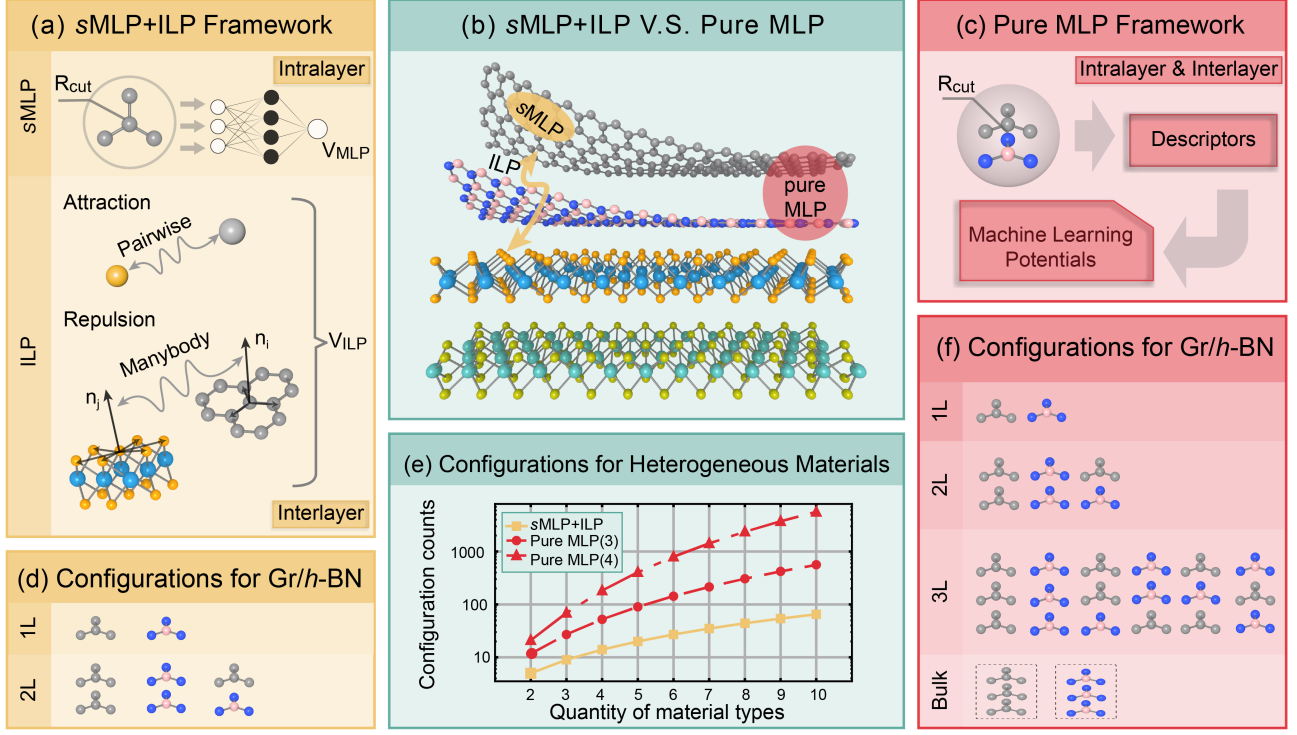


FIG. 1. Schematic architecture of sMLP+ILP and pure MLP framework. (a)–(c) Schematic illustration of the architecture of (a) sMLP+ILP and (c) pure MLP as well as (b) their comparison. In the sMLP+ILP framework, the MLP is designed to capture the 2D local chemical environment within a monolayer, while the ILP accounts for long-range pairwise and many-body interactions across different layers. In contrast, the pure MLP framework learns descriptors from a more complex 3D local chemical environment across layers, and thus must consider more atoms within the same layer and complex combinations of vdW materials. (d)–(f) Comparison of the ideal training configuration numbers for both frameworks. (d) and (f) is the number training configurations for the Gr/h-BN heterostructure in the sMLP+ILP framework and pure MLP(3) framework, respectively. (e) shows the number of required configurations as a function of the number of distinct monolayer components. For pure MLP approach, $N_{\text{MLP}(3)}$ and $N_{\text{MLP}(4)}$ represent the number of required configurations based on the assumption that up to three layers (see Eq. 11) and four layers (see Eq. 12) are necessary to accurately describe the surface and interface environment.

in different layers from atom i using a cutoff of $R_{\text{cut}}^{\text{ILP}}$. In practical implementation, atoms with different molecule IDs in LAMMPS or group labels in GPUMD are used to distinguish atoms belonging to different layers [36, 83].

The sMLP term focuses on the intralayer interactions, when k equals to l , for covalent bonds, which can be expressed using a neural network (NN):

$$V_{kl}^{\text{sMLP}} \delta_{kl} = V_{kk}^{\text{sMLP}} = \sum_{i \in \Omega^k} f_{\text{NN}}(q_1^i, q_2^i, \dots, q_{N_{\text{des}}}^i), \quad (2)$$

where Ω^k is the set of atoms in the k^{th} layer, $f_{\text{NN}}(\cdot)$ represents the NN operations and $\{q_\nu^i\}$ is a set of descriptors that encode local environment messages information, including atomic positions and elements from the neighbors of atom i . This transformation can be expressed as:

$$q_\nu^i = \sum_{j \in \Omega_i^{\text{sMLP}}} g_\nu(\mathbf{r}_{ij}) \quad (3)$$

where $\{g_\nu\}$ is a set of descriptor functions, and \mathbf{r}_{ij} is

the position vector from atom i to atom j . Since the intralayer interactions typically require a small cutoff, many MLPs can accurately describe them. In this work, we adopt the NEP framework, which provides an efficient and accurate description of covalent bond interactions in monolayer 2D materials within our sMLP+ILP approach. Specifically, following the pioneering Behler and Parrinello approach [61], the NEP uses a single hidden NN layer to compute the site energy V_{kk}^{sMLP} [67]:

$$V_{kk}^{\text{sMLP}} = \sum_{i \in \Omega^k} \left[\sum_{\mu=1}^{N_{\text{neu}}} w_\mu^{[1]} \tanh \left(\sum_{\nu=1}^{N_{\text{des}}} w_{\mu\nu}^{[0]} q_\nu^i - b_\mu^{[0]} \right) - b^{[1]} \right], \quad (4)$$

where $w_{\mu\nu}^{[0]}$, $w_\mu^{[1]}$, $b_\mu^{[0]}$, $b^{[1]}$ are trainable weights and biases of the NN, N_{neu} is the number of neurons in the hidden layer, N_{des} is the number of descriptors and $\tanh(\cdot)$ is the activation function. The NEP descriptors consist of radial and angular components. The two-body radial

descriptors $q_n^i (0 \leq n \leq n_{\max}^R)$ are constructed as

$$q_n^i = \sum_{j \in \Omega_i^{s\text{MLP}}} g_n(r_{ij}), \quad (5)$$

where r_{ij} is the distance between atom i and atom j , g_n is the n th expansion radial descriptor function. The many-body angular descriptors q_{nl}^i can be expressed as

$$q_{nl}^i = \sum \sum_{j,k \in \Omega_i^{s\text{MLP}}} g_n(r_{ij}) g_n(r_{ik}) P_l(\theta_{ijk}), \quad (6)$$

where $P_l(\cdot)$ is the Legendre polynomial of order l and θ_{ijk} is the angle for the triplet (ijk) with atom i in the center.

The interlayer interactions are represented by ILP term, which includes a long-range dispersion attraction term and Pauli repulsion term [34]:

$$V_{kl}^{\text{ILP}}(1 - \delta_{kl}) = \sum_{i \in \Omega^k} \sum_{j \in \Omega^l \cap \Omega_i^{\text{ILP}}} \sum_{l \neq k} \text{Tap}(r_{ij}) [V^{\text{att}}(r_{ij}) + V^{\text{rep}}(r_{ij}, \mathbf{n}_i, \mathbf{n}_j)], \quad (7)$$

where $\text{Tap}(\cdot)$ is a long-range taper function of distance, $\text{Tap}(r_{ij}) = 20 \left(\frac{r_{ij}}{R_{\text{cut}}} \right)^7 - 70 \left(\frac{r_{ij}}{R_{\text{cut}}} \right)^6 + 84 \left(\frac{r_{ij}}{R_{\text{cut}}} \right)^5 - 35 \left(\frac{r_{ij}}{R_{\text{cut}}} \right)^4 + 1$. Previous work has indicated that interlayer Coulomb interactions are significantly weaker than vdW forces [38], thus Coulomb contributions were omitted from the ILP formula of Eq. 7 to improve computational efficiency. The attraction term adopts a dispersion correction similar to Tkatchenko and Scheffler's approach [40] for augmenting standard DFT exchange-correlation functionals:

$$V^{\text{att}}(r_{ij}) = - \frac{1}{1 + e^{-d_{ij}[r_{ij}/(S_{R,ij} \cdot r_{ij}^{\text{eff}}) - 1]}} \frac{C_{6,ij}}{r_{ij}^6}. \quad (8)$$

The repulsion term follows Kolmogorov and Crespi's approach [30, 33], using a Morse-like exponential isotropic term with an anisotropic correction:

$$V^{\text{rep}}(r_{ij}, \mathbf{n}_i, \mathbf{n}_j) = e^{\alpha_{ij} \left(1 - \frac{\gamma_{ij}}{\rho_{ij}} \right)} \left\{ \epsilon_{ij} + C_{ij} \left[e^{-\left(\frac{\rho_{ij}}{\gamma_{ij}} \right)^2} + e^{-\left(\frac{\rho_{ji}}{\gamma_{ij}} \right)^2} \right] \right\}. \quad (9)$$

Here ρ_{ij} and ρ_{ji} are the lateral interatomic distance, which can be expressed as:

$$\begin{cases} \rho_{ij}^2 = r_{ij}^2 - (\mathbf{r}_{ij} \cdot \mathbf{n}_i)^2 \\ \rho_{ji}^2 = r_{ij}^2 - (\mathbf{r}_{ij} \cdot \mathbf{n}_j)^2 \end{cases} \quad (10)$$

where \mathbf{n}_i is the local normal vector of atoms i , defined as the normal to the plane formed by its nearest directly bonded neighbors, with the remaining parameters being fitting parameters.

We note that the definition of the normal vector may vary depending on the specific vdW interface. Figure 1(a) illustrates the normal vector (\mathbf{n}_i) definitions for Gr and MoS₂. For Gr and *h*-BN, which have single-atom thickness, the normal vector is defined based on up to three nearest in-plane neighbors [30, 33]. For MoS₂, which has a sandwich-like layered structure, it is determined using up to six nearest neighbors within the outermost sulfur sublayer [37]. In GPUMD, we adopt the algorithm from the optimized version of ILP in LAMMPS to couple the neighbor lists of ILP and NEP [84]. As ILP only considers the nearest neighbor atoms when computing normal vectors, we utilize the radial neighbor list of NEP to reduce computational cost.

B. Comparison with existing approaches

In this section, we discuss various existing potential approaches for vdW materials and highlight the necessity of *s*MLP+ILP approach, particularly for accurately modeling complex multilayer heterostructures. Numerous MLPs have now been developed to simulate the vdW materials to achieve (near) *ab initio* accuracy, aiming to capture both interlayer and intralayer interactions within a single NN framework (see Figure 1(c)). While most MLPs can theoretically simulate vdW materials in this manner, two significant challenges arise, as discussed below.

The first challenge is how to determine an optimal cutoff for MLPs that capture long-range vdW interactions while maintaining comparable efficiency, as these vdW interactions can extend through several interlayer spacings and have significant impacts on structural reconstructions [42] and corresponding physical properties [10]. For example, the interlayer distance of MoS₂ is 6.0 Å, so a cutoff of at least 12.0 Å should be set to include the forces from the next-nearest layers. However, larger cutoffs result in reduced computational efficiency while not necessarily guaranteeing improved accuracy. This is shown in the NEP model case for bilayer graphene [76], where the NEP using a radial cutoff of 10 Å exhibited a larger force root mean square error (RMSE) than that of 10 Å with identical model setup, while achieving only about half the computational speed. As pure MLP approaches don't inherently distinguish between intralayer and interlayer interactions from a physical perspective, implementing them with longer cutoffs forces these MLPs to incorporate numerous additional features into local atomic environments, significantly complicating the training process. Consequently, extending cutoffs beyond 1 nm for pure MLPs to capture long-range vdW interactions from next-nearest layers not only dramatically reduces computational efficiency but can paradoxically lead to decreased accuracy rather than improvement. To resolve this dilemma, the DFT-D3 dispersion energy correction term [85] has been combined with MLPs [76, 86], allowing the MLPs to focus on local chemical environments while

the DFT-D3 handles long-range dispersion interactions.

The second key issue concerns large number of training configurations required for heterostructures composed of various monolayer components. MLPs rely on the invariant or equivariant descriptors to transform the spatial coordinates to local chemical information, allowing them to learn from discrete training points and predict a smooth, high-dimensional PES in an interpolative manner based on electronic data obtained from *ab initio* calculations. Theoretically, achieving high accuracy and reliability requires the training dataset to comprehensively cover all configurations that may arise during MD simulations. Furthermore, for vdW heterostructures, local chemical environment can extend beyond the nearest layers and vary with different stacking configurations. For the Gr/*h*-BN heterostructure within the pure NEP framework, it has been demonstrated that at least 13 configurations [74], including 2D structures with up to three layers and bulk structures, are required to accurately capture the surface, interface, and bulk chemical environment of this system, as shown in Figure 1(f). Building on the assumption that at least three layers are necessary to capture the interface and surface environment, the total number of configurations required for simulating vdW heterostructures with n distinct monolayer components can be determined as follows. The number of monolayer configurations is C_n^1 . The number of bilayer homostructures is also C_n^1 , while the number of bilayer heterostructures, considering all component pairs, is C_n^2 . For trilayer configurations, the total count is $C_n^1 + 4C_n^2 + 3C_n^3$ (see Supporting Information (SI) Section S1 for details). Finally, the number of bulk configurations is also C_n^1 . Summing all these contributions, the minimum number of required configurations is given by

$$N_{\text{MLP}(3)} = \frac{1}{2}n^3 + n^2 + \frac{5}{2}n \sim O(n^3) \quad (11)$$

Furthermore, if we assume that up to four layers are necessary to fully cover the surface and interface environment, the total number of required configurations increases to

$$N_{\text{MLP}(4)} = \frac{1}{2}n^4 + \frac{1}{2}n^3 + \frac{3}{2}n^2 + \frac{5}{2}n \sim O(n^4) \quad (12)$$

where the detailed derivation is provided in SI Section S1.

However, for *s*MLP+ILP framework, which fully decouples the interlayer and intralayer interactions (see Figure 1(b)), it is sufficient to prepare only C_n^1 monolayer configurations for the MLP, whereas C_n^1 bilayer homogeneous and C_n^2 bilayer heterogeneous configurations are required for ILP. This results in a total number of required configurations given by

$$N_{\text{ILP}} = \frac{1}{2}n^2 + \frac{3}{2}n \sim O(n^2) \quad (13)$$

In Figure 1(d) we show that only five configurations are required in the *s*MLP+ILP framework for Gr/*h*-BN

heterostructure system. Figure 1(e) compares the number of required training configurations between existing pure MLP approach and the proposed *s*MLP+ILP framework. For an extremely complex vdW heterostructure containing 10 distinct monolayer components, the number of required reference configurations for $N_{\text{MLP}(4)}$ is approximately 100 times larger than that for *s*MLP+ILP. Moreover, the pure MLP dataset includes configurations with significantly more atoms, leading to a computational cost for electronic data calculations that could be several orders of magnitude higher. Additionally, for a given set of fixed configurations, the relatively sliding PESs in multilayer systems become significantly more complex, necessitating extensive sampling of reference structures.

C. Validation and benchmark

1. High accuracy of *s*MLP models

In this work, we employed the *s*MLP + ILP framework to investigate homogeneous and heterogeneous vdW systems composed of one, two, or all three components from the monolayers Gr, *h*-BN, and MoS₂. Interlayer interactions between Gr, *h*-BN, and their heterostructures were modeled using the ILP approach from Ref. [36]. Similarly, interactions between both Gr/MoS₂ and *h*-BN/MoS₂ were described by the ILP model from Ref. [39]. These ILP models are grounded in the electronic nature of weak interlayer interactions and are fitted to state-of-the-art DFT data augmented by nonlocal many-body dispersive (MBD-NL) corrections [92]. As a result, they accurately capture binding energy curves and sliding PESs, achieving first-principles accuracy with energy RMSEs on the order of 0.1 meV/atom [33–36, 39]. As the necessary ILP models are already available, in this section we focus solely on developing three *s*MLPs, corresponding to the individual monolayer components.

To train the MLPs, we first prepared a reference dataset consisting of energies, atomic forces, and virials obtained from DFT calculations at the exchange-correlation Perdew-Burke-Ernzerhof (PBE) level [93] (see Section IV A for details). For Gr and *h*-BN, both extended and edge configurations were included, with hydrogen passivation effects explicitly considered for the edge structures. In contrast, only pristine, fully periodic configurations were considered for MoS₂ (see SI, Section S2 for details). For each monolayer, reference structures were generated through random perturbations and MD simulations at finite temperatures (see Section IV B).

Once the reference dataset was prepared, the third generation of NEP framework [67, 79, 80], as implemented in GPUMD, was used to train Gr *s*MLP and the fourth generation of NEP framework [94] was used to train *h*-BN and MoS₂ *s*MLPs. The NEP framework employs a simple feedforward NN to represent the site energy of an atom (see Eq. 4), using descriptor vectors composed of a number of radial (see Eq. 5) and angular (see Eq. 6)

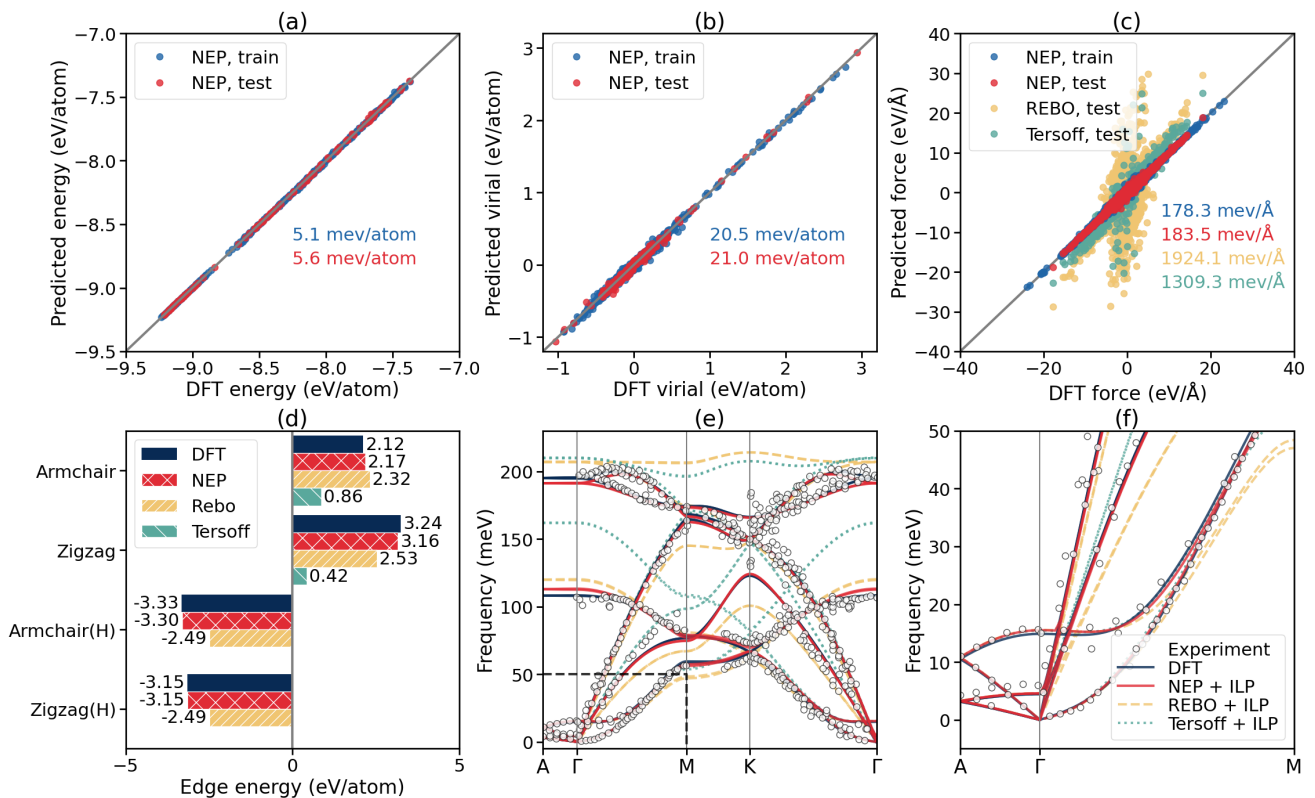


FIG. 2. (a)-(c) Parity plots for energy, virial, and force comparing DFT reference data and NEP predictions for the whole training and testing dataset. In (c), there are also REBO and Tersoff predictions for testing dataset. (d) Edge energy calculated by DFT, NEP, REBO, Tersoff for monolayer graphene structures showed in SI. (e)-(f) Phonon spectra of bulk graphite. The solid red lines, dashed blue lines, and dashed-dotted green lines are dispersion curves calculated using the NEP+ILP, REBO+ILP and Tersoff+ILP force fields, respectively. Experimental result [87] of bulk graphite is given by open black circles. (f) shows a zoom-in of the low-energy phonon modes around the Γ -point.

components. The separable natural evolution strategy (SNES) [95] was used for the optimization of the parameters in NEP models. For all sMLP models, a consistent cutoff of 5 \AA was used for both radial and angular descriptor components. Additionally, the weight for virial RMSE term was set as 0.5 to improve the accuracy of NEP model in predicting the mechanical properties [60]. Full details of the NEP training procedure are provided in SI Section S3.

Figure 2(a)-(c) show the energy, virial, and force predictions for Gr obtained from the sMLP model, compared against the DFT reference values. Each panel also reports the corresponding RMSEs for both the training and test datasets. The NEP model demonstrates high accuracy in predicting the energy, virial and forces, with RMSE values below 6.0 meV/atom , 21 meV/atom , and 184 meV/\AA , respectively, for both datasets. A comparable level of accuracy is achieved for *h*-BN, while even higher accuracy is observed for MoS_2 (see SI Figure S4), as its reference dataset does not include edge structures. For comparison, in Figure 2(c) we also evaluate the accuracy of two widely used empirical potentials, i.e., the Tersoff potential [23] and the REBO potential [21], by com-

paring their predicted forces on the test dataset against the DFT reference values. It is clear that the NEP model, with an RMSE of 183.5 meV/\AA , exhibits significantly higher accuracy than the other two empirical potentials, whose predictions deviate substantially from the parity line, with corresponding RMSE values exceeding 1000 meV/\AA .

Beyond the RMSE values, we further evaluated the predictive accuracy of the NEP and the two empirical potentials by comparing their predicted edge energies of Gr and *h*-BN monolayers against DFT reference results. The edge energy of a monolayer, V_{EE} , is calculated as

$$V_{EE} = V_{PBC} - V_{nPBC} \quad (14)$$

where V_{PBC} and V_{nPBC} represent the energies of the monolayer without edges under periodic boundary conditions and that with edges under non-periodic boundary conditions, respectively (see SI Section S5 for details). Since the Tersoff potential does not support hydrogen atoms, it is only applied to non-hydrogenated structures. As shown in Figure 2(d) and SI Figure S5, the edge energies of both Gr and *h*-BN computed using the NEP model align closely with the DFT reference values, ex-

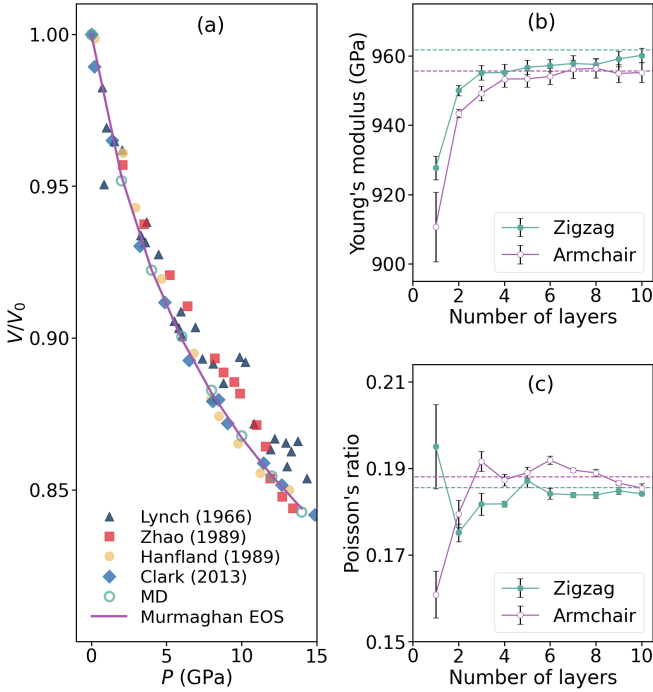


FIG. 3. (a) Pressure (P) dependence of the normalized volume (V/V_0 , V/V_0) of bulk graphite, where V and V_0 represent the pressure-dependent and initial volumes, respectively. The green hollow circles represent MD simulation results using the s MLP+ILP model. The solid purple line is the fitted curve using the Murnaghan EOS; the fitted curves from the two additional EOSs coincide closely and are therefore not shown. Blue triangles, red squares, yellow circles and blue diamond represent experimental data obtained from Ref. [88], Ref. [89], Ref. [90], and Ref. [91], respectively. (b) Young's modulus and (c) Poisson's ratio of the Gr system as functions of the number of layers, predicted by s MLP+ILP-based MD simulations. Results (dashed line) for bulk graphite are also included for comparison.

hibiting errors on the order of 0.01 eV/atom, which are one to two orders of magnitude smaller than those obtained with two empirical potentials. The high accuracy in predicting energy, atomic forces, virials, and edge energies demonstrates the reliability of the developed s MLPs in describing intralayer interactions in all three monolayers.

2. Accuracy of the s MLP+ILP models in predicting phonon and mechanical properties of graphite

After demonstrating the accuracy of MLPs in describing intralayer interactions in monolayers, we now take bulk graphite as an example to further benchmark the accuracy of the s MLP+ILP approach in describing both phonon and mechanical properties.

To this end, we used s MLP+ILP to compute the phonon dispersion curves of bulk graphite at zero pres-

TABLE I. Bulk modulus (B), zero-pressure derivative (B'), intralayer lattice constant (a_0), and interlayer lattice constant (c_0) of bulk graphite, calculated from MD simulations using the s MLP+ILP model and compared with experimental data from X-ray diffraction [88–90]. Values in parentheses represent statistical errors. For the MD results, three different EOSs [90, 96–100] (see SI Section S4 for details) were used to fit B and B' . a_0 and c_0 of MD are computed in 0 K.

Method	B (GPa)	B'	a_0 (Å)	c_0 (Å)
Experiment (Ref. [88])	32(2)	12.3(0.7)	2.4612	6.7078
Experiment (Ref. [90])	33.8(0.3)	8.9(0.1)	2.603	6.706
Experiment (Ref. [89])	30.8(2.0)	–	2.462	6.707
MD (Murnaghan)	32.9(1.7)	9.6(0.6)		
MD (Birch-Murn.)	28.9(0.6)	15.2(0.5)	2.4671	6.726
MD (Vinet)	31.8(1.1)	11.4(0.5)		

sure and temperature by diagonalizing the dynamical matrix in LAMMPS. The results were compared with those obtained from REBO+ILP, Tersoff+ILP, DFT calculations, as well as experimental measurements [87]. As shown in Figure 2(e)-(f), the s MLP+ILP approach accurately reproduces the dispersion of both the low-energy out-of-plane branches near the Γ point and the high-energy branches along the $\Gamma \rightarrow M \rightarrow K \rightarrow \Gamma$ path. In contrast, significant discrepancies observed in the high-energy modes for both the REBO+ILP and Tersoff+ILP models stem from limitations in their intralayer potential descriptions. Notably, the s MLP+ILP curve closely matches the DFT results, further confirming that this approach can achieve DFT-level accuracy.

To further evaluate the s MLP+ILP performance in describing mechanical properties under hydrostatic pressure, we performed MD simulations to compute its bulk modulus and compared the results with available experimental data [88–91]. As shown in Figure 3(a), the computed pressure–volume (P – V) relationship from our simulations aligns well with experimental measurements. The bulk moduli (B) and zero-pressure derivatives (B') of bulk graphite, obtained by fitting three different EOSs (see SI Section S4 for details), respectively, fall within the range of 28 GPa to 33 GPa and 9 GPa to 16 GPa (see Table I). Moreover, our MD simulations show good agreement with the experimental values of the intra- and interlayer lattice constants. The deviations between simulation and experiment are approximately 0.01 Å for the intralayer and 0.02 Å for the interlayer lattice constants, except for one reported experimental value of 2.603 Å, which significantly overestimates the intralayer lattice constant. Overall, these results demonstrate that the s MLP+ILP approach provides a robust and reliable description of the bulk properties of graphite across a wide range of external pressures.

Next, we validate the s MLP+ILP approach by calculating the elastic constants of the graphite system with varying number of layers. The Young's modulus and

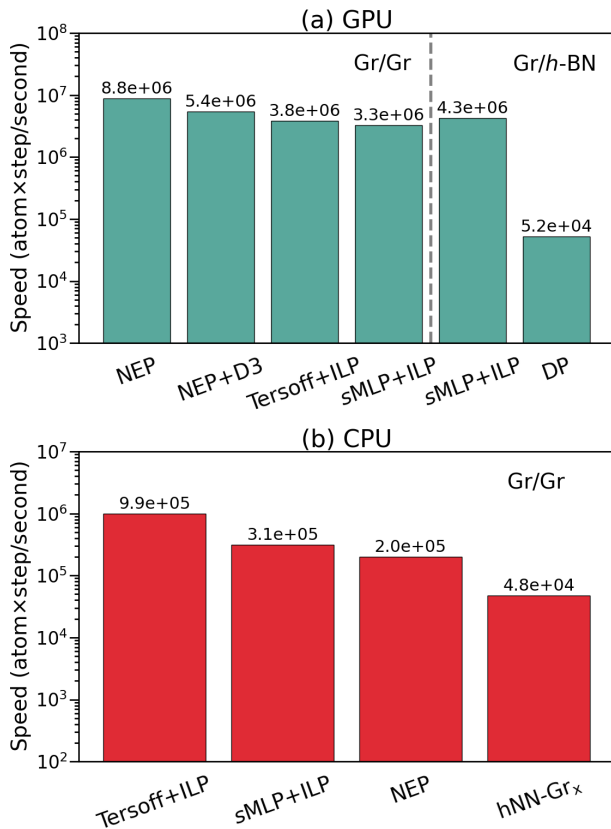


FIG. 4. Computational speeds for the *sMLP+ILP* approach implemented in (a) GPUMD using GPU and (b) LAMMPS using CPU. Benchmarks were conducted on both Gr/Gr system (containing 294,912 atoms for GPU tests and 4,608 atoms for CPU tests) and Gr/*h*-BN systems (containing 6,400 atoms). The performance for other potential models and hybrid approaches are also included for comparison.

Poisson’s ratio for monolayer Gr have been experimentally measured to be approximately 1 TPa and 0.17, respectively [101]. Similarly, Blakslee et al. reported values for bulk graphite of 1.02 ± 0.03 TPa for the Young’s modulus and 0.16 ± 0.06 for the Poisson’s ratio, based on static tensile and compression measurements [102]. Here, we calculated Young’s modulus and Poisson’s ratio by applying uniaxial tension along armchair and zigzag directions using *sMLP+ILP* model (see Section IV C for details). For a monolayer Gr, the Poisson’s ratio was predicted to be 0.161 and 0.195 in the armchair and zigzag directions, respectively, while the corresponding Young’s moduli were 0.911 TPa and 0.928 TPa, respectively, indicating a weak elastic anisotropy. As the number of layers increases, the predicted Young’s modulus rises and gradually converges to the bulk graphite value. Meanwhile, the anisotropy in the Poisson’s ratio diminishes with increasing thickness. Notably, our *sMLP+ILP* predictions for both monolayer Gr and bulk graphite are consistent

with experimental values [101, 102]. Additional results and comparisons with other potential models are provided in SI Section S5.

3. Efficiency of the *sMLP+ILP* approach

The *sMLP+ILP* approach not only enhances accuracy but also maintains high computational efficiency compared to the existing pure MLPs and hybrid empirical potential +ILP methods. In this section, we benchmark its performance against several representative approaches, including Tersoff+ILP, NEP+D3 [76], and a set of existing MLP models: NEP [76], deep potential (DP) [75], and hNN-Gr_x [77].

To accurately capture the decay of binding energy with interlayer distance in vdW interfaces, the ILP model employs a cutoff of 16 Å, while the pure NEP model [76] uses a radial cutoff of 10 Å and an angular cutoff of 4.5 Å. For the NEP+D3 approach [76], both radial and angular cutoffs are set to 4.5 Å, with an additional 16 Å cutoff for the D3 correction. The cutoffs used in the DP and hNN-Gr_x models are all no longer than 10 Å.

As shown in Figure 4, we benchmarked these approaches on both GPU and CPU platforms, using a single NVIDIA GeForce RTX 4090 GPU and 36 Intel Xeon 6240 CPU cores, respectively. All GPU-based tests were conducted using GPUMD (version 3.9.5), except for the DP model, which was tested using LAMMPS (stable release, 29 August 2024). All CPU-based tests were also run using LAMMPS (stable release, 29 August 2024) and we use the OPT version of ILP potential in LAMMPS [84]. Two types of vdW bilayers were considered: Gr/Gr homostructures and Gr/*h*-BN heterostructures. For each test, simulations were performed in the microcanonical ensemble for 1,000 steps with a time step of 1 fs. Notably, on a single desktop GPU, the *sMLP+ILP* approach achieves a computational speed ranging from 3×10^6 to 5×10^6 atom step/s, comparable to that of the pure NEP, NEP+D3, and Tersoff+ILP models, and approximately two orders of magnitude faster than the DP model. On the CPU platform, the *sMLP+ILP* performance (3.1×10^5 atom step/s) is similarly close to Tersoff+ILP and pure NEP models, and one order of magnitude faster than other MLPs models. Our results also highlight the high computational efficiency of the NEP approach, which is a key reason we adopted it to train the *sMLP* model in our hybrid MLP+ILP framework.

D. Moiré superlattices in complex vdW heterostructures

1. Comparison with Experimental Moiré Patterns

Having demonstrated the accuracy and efficiency of our *sMLP+ILP* approach, we now apply it in large-scale

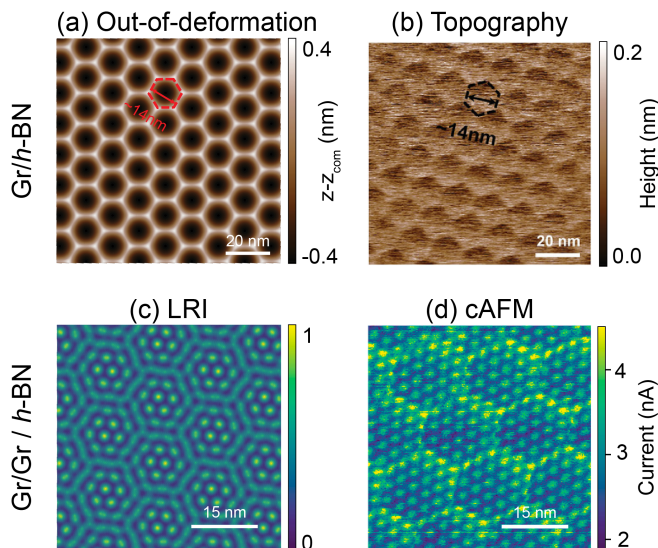


FIG. 5. (a) *sMLP* + *ILP* predicted out-of-plane deformation predicted and (b) experimentally measured topography of a relaxed *Gr/h-BN* heterostructure. (c) *sMLP* + *ILP* predicted LRI map and (d) experimentally measured conductive atomic force microscopy image of a relaxed *Gr/Gr/h-BN* heterostructure with a 4.2° twist angle between *Gr* layers. Panels (b) is adapted with permission from Ref. [46]. Copyright 2022, Wiley. Panel (d) is adapted with permission from Ref. [103]. Copyright 2021, American chemistry Society.

atomistic simulations to explore structural reconstruction in complex vdW systems. Previous studies have showed that certain multilayer vdW materials undergo local reconstruction, forming Moiré out-of-plane distortions to maximize the overall areas corresponding to the energetically favorable (commensurate) stacking mode [2, 42]. The emergence of Moiré superlattices involves the formation of sharp domain walls of unfavorable stacking between nearly commensurate regions, which relieve excess in-plane stress induced by interlayer lattice mismatch.

Herein, we demonstrate the advantage of *sMLP*+*ILP* approach in modeling complex heterostructures by predicting the Moiré patterns in both *Gr/h-BN* bilayer and *Gr/Gr/h-BN* trilayer. For both systems, the experimental measurements of Moiré superlattices are available [46, 103], enabling direct validation of our predictions. To that end, we constructed *Gr* (56×56)/*h-BN* (55×55) heterojunction models (containing 36,352 atoms) to explicitly eliminate the 1.8% lattice mismatch between the two monolayers. Beyond this intrinsic lattice mismatch, a twisted angle of 4.2° was applied to the top two *Gr* layers and 0.04° to the middle *Gr* and *h-BN* in the trilayer system to match the experimental setup, resulting in a *Gr* (52×59)/*Gr* (59×52)/*h-BN* (58×51) heterojunction model (containing 54,858 atoms).

Initially, the models exhibit high stress at the boundaries, necessitating relaxation. We achieve this through energy minimization described in Section IV D. With a

force convergence criterion below 1×10^{-6} eV/Å, we obtained the optimized Moiré superlattices shown in Figure 5, and compared them with experimental observations. For the *Gr* (56×56)/*h-BN* (55×55) system, a hexagonal Moiré superlattice with a periodicity of 14 nm emerges due to the intrinsic lattice mismatch between *Gr* and *h-BN* (Figure 5(a)), in excellent agreement with the experimentally measured topography [46] (Figure 5(b)). For the *Gr* (52×59)/*Gr* (59×52)/*h-BN* (58×51) system, we employed the local registry index (LRI) method (see SI Section S7 for details) [104], which characterizes the local stacking configurations for the optimized superlattice. As shown in Figure 5(c), the *sMLP*+*ILP* model predicts a double-Moiré pattern: a larger 14 nm pattern arising from the *Gr/h-BN* lattice mismatch, and a smaller one originating from the lattice mismatch between twisted *Gr/Gr* interface. This prediction closely resembles the experimental Moiré superlattice observed via the conductive atomic force microscopy [103] (Figure 5(d)).

2. Stacking order-dependent Moiré superlattices in *Gr/h-BN/MoS₂* heterostructures

Building on the successful reproduction of experimental Moiré superlattices in *Gr/h-BN* systems, we extend the *sMLP*+*ILP* approach to predict Moiré patterns in more complex vdW heterostructures composed of *Gr*, *h-BN*, and *MoS₂*. Considering the intrinsic lattice mismatches of 1.8% between *Gr* and *h-BN*, and 29.1% between *Gr* and *MoS₂*, we constructed *Gr*(111×111)/*h-BN*(109×109)/*MoS₂*(86×86) heterojunction models (containing 423,552 atoms), exhibiting lattice mismatch in each layer reduced to below 0.05%. To examine stacking-order-dependent reconstruction behavior, we considered three configurations: *Gr/MoS₂/h-BN*, *h-BN/Gr/MoS₂*, and *MoS₂/h-BN/Gr*. The initial interlayer spacing was set to the equilibrium value of the corresponding bilayers (see SI Section S6 for details). All trilayer heterostructure models were optimized using the same procedure as the *Gr/h-BN* system (see Section IV D for details).

Figure 6(a-c) show the relative out-of-plane deformations of each component monolayer in *h-BN/Gr/MoS₂*, *MoS₂/h-BN/Gr* and *Gr/MoS₂/h-BN* heterostructures. When the *Gr* and *h-BN* are adjacent (see Figure 6(a) and (b)), the deformation is dominated by their interlayer interaction, giving rise to a Moiré pattern with a periodicity of approximately 14 nm. In contrast, when the *MoS₂* layer is inserted between *Gr* and *h-BN* (see Figure 6(a)), the deformation is suppressed by nearly two orders of magnitude, leading to atomically flat interfaces with negligible out-of-plane corrugation. This stacking-order-dependent suppression aligns well with recent experimental observations [105].

To understand why different stacking orders lead to distinct Moiré superlattices, we calculated the weighted mean energy of each atom by summing the energies of

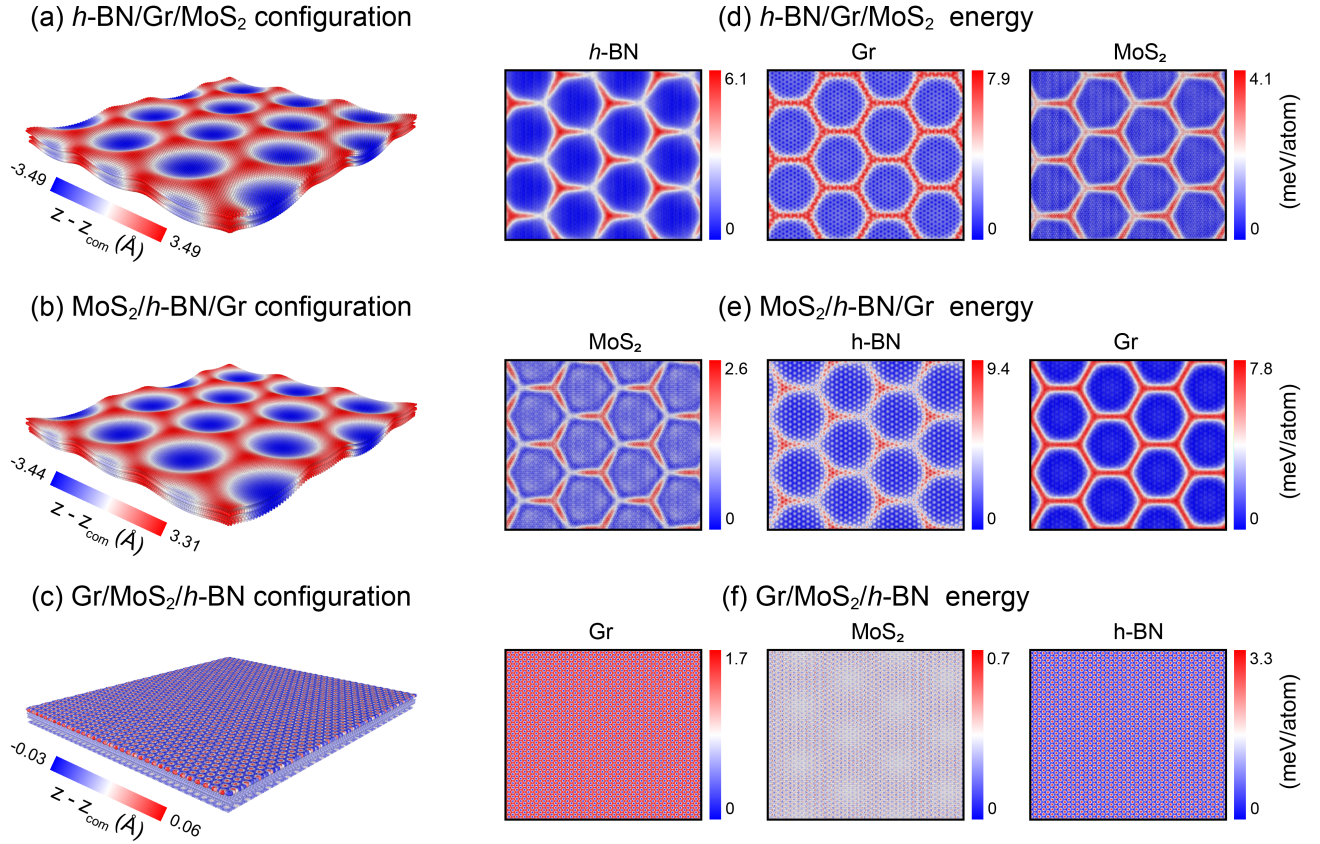


FIG. 6. (a-c) Out-of-plane deformation and (d-e) energy distribution of the optimized $h\text{-BN}/\text{Gr}/\text{MoS}_2$ (top), $\text{MoS}_2/h\text{-BN}/\text{Gr}$ (middle), and $\text{Gr}/\text{MoS}_2/h\text{-BN}$ (bottom) structures. Panels (d-e) present the weighted atomic energy maps for each component monolayer in the optimized vdW heterostructures, with all values presented relative to the corresponding minimum energy of the respective layer.

its neighbor atoms within three nearest hexagonal rings (see SI Section S6 for details), effectively reflecting the local stacking environments. Figure 6(d-f) present the weighted atomic energy maps for each monolayer layer in $h\text{-BN}/\text{Gr}/\text{MoS}_2$, $\text{MoS}_2/h\text{-BN}/\text{Gr}$ and $\text{Gr}/\text{MoS}_2/h\text{-BN}$ heterostructures, respectively.

For $h\text{-BN}/\text{Gr}/\text{MoS}_2$ and $\text{MoS}_2/h\text{-BN}/\text{Gr}$ system, the energy Moiré patterns of Gr and $h\text{-BN}$ are dominated by a 14 nm hexagonal supercell. Although smaller-scale Moiré features appear in the layers adjacent to the MoS_2 layer (Gr layer in Figure 6(d) and $h\text{-BN}$ layer in Figure 6 (e)), their energy corrugations are substantially weaker compared to those associated with the larger 14 nm pattern. To minimize the overall energy, energetically favorable stacking (commensurate) regions expand by compressing the incommensurate areas, thereby inducing out-of-plane deformation to alleviate the in-plane stress. In both the $h\text{-BN}/\text{Gr}/\text{MoS}_2$ and $\text{MoS}_2/h\text{-BN}/\text{Gr}$ systems, the initial energy corrugation of the MoS_2 monolayer is minimal, exhibiting only weak Moiré modulations (see SI Figure S7). As a result, it cannot compete with the stronger interlayer interaction between Gr and $h\text{-BN}$, and is thus forced to conform, presenting

a similar 14 nm hexagonal Moiré superlattice.

In contrast, the $\text{Gr}/\text{MoS}_2/h\text{-BN}$ structure exhibits no pronounced Moiré pattern in the Gr and $h\text{-BN}$ layers, as the presence of the intervening MoS_2 layer significantly increases their separation, weakening the interlayer interactions. As a result, during energy minimization, the high-energy stacking regions in each layer cannot contract effectively. This leads to a substantial suppression of out-of-plane deformation—nearly two orders of magnitude lower than that observed in the $h\text{-BN}/\text{Gr}/\text{MoS}_2$ and $\text{MoS}_2/h\text{-BN}/\text{Gr}$ structures.

III. CONCLUSIONS

In conclusion, we present a hybrid modeling framework, $s\text{MLP}+\text{ILP}$, for simulating vdW materials, especially complex heterostructures. In this approach, the $s\text{MLP}$, with a large number of parameters, is dedicated to capturing short-range intralayer interactions, while the ILP , with minimal parameterization, efficiently describes all long-range interlayer interactions. By assigning distinct interlayer and intralayer interactions to separate po-

tential components, this hybrid framework enhances simulation accuracy without sacrificing computational efficiency. Moreover, the *s*MLP+ILP approach significantly reduces the required training dataset by at least an order of magnitude compared to fully machine-learned models, enabling faster and more accessible training for complex heterostructures.

To realize this framework, we employed NEP as the *s*MLP component and enabled its seamless integration with the ILP model in both LAMMPS and GPUMD, achieving comparable computational efficiency with empirical potentials. Notably, our framework achieves a remarkable speed of over 2×10^6 atom \cdot step/s in GPUMD on a single NVIDIA RTX 4090 desktop GPU when simulating complex trilayer vdW heterostructures with 423,552 atoms. Validated on monolayer Gr, *h*-BN, and MoS₂, the trained *s*MLP models yield force RMSEs an order of magnitude lower than empirical potentials. Edge energy errors for monolayer Gr and *h*-BN are reduced to 0.01 eV/atom, compared to 0.1 eV/atom to 1 eV/atom for REBO and Tersoff. The *s*MLP+ILP framework also reproduces the phonon spectrum and mechanical properties of graphite in close agreement with DFT and experimental results, confirming its accuracy, transferability, and efficiency for simulating complex vdW heterostructures.

Finally, we applied the *s*MLP+ILP framework to investigate the emergence of Moiré superlattices in complex vdW heterostructures composed of Gr, *h*-BN, and MoS₂ monolayers. For both bilayer Gr/*h*-BN and twisted trilayer Gr/Gr/*h*-BN systems, the framework successfully reproduces Moiré patterns in excellent agreement with experimental observations. Building on this, we further explored how stacking order affects structural reconstruction in trilayer Gr/*h*-BN/MoS₂ systems, where interlayer interactions between Gr and *h*-BN layers play a key role. When these two layers are adjacent, the system exhibits pronounced out-of-plane hexagonal corrugation of 3 Å to 5 Å, preserving the characteristic 14 nm Moiré periodicity seen in bilayer Gr/*h*-BN. In contrast, when the MoS₂ layer is inserted between Gr and *h*-BN, their interaction becomes effectively decoupled, resulting in a significant suppression of deformation to less than 0.1 Å, and the Moiré pattern disappears.

These findings demonstrate the strong predictive capability and broad applicability of the *s*MLP+ILP approach for modeling large-scale vdW heterostructures. By combining high accuracy with computational efficiency, this framework is particularly well-suited for investigating key physical phenomena such as thermal transport, interfacial friction, and sliding ferroelectricity in complex layered systems.

IV. METHOD

A. DFT calculations

All DFT calculations for NEP model and edge energy were performed using the Vienna Ab initio Simulation Package [106, 107] with the Perdew–Burke–Ernzerhof [93] exchange–correlation functional within the projector augmented wave [108] framework. For the electronic self-consistent loop, we set a threshold of 1×10^{-7} eV with an energy cutoff of 850 eV. A Gaussian smearing width of 0.1 eV was employed. A sufficiently large vacuum spacing for all monolayer systems was applied along the out-of-plane direction to eliminate spurious interactions between periodic images. Due to differences in the supercell sizes, distinct *k*-point sampling schemes were employed. For the Gr and *h*-BN systems, a $3 \times 3 \times 1$ Monkhorst–Pack grid was adopted. In contrast, for the MoS₂ system, the Brillouin zone was sampled using a Γ -centered mesh with a reciprocal-space resolution of 0.15 \AA^{-1} .

B. Reference datasets

We prepared separate reference datasets to develop *s*MLPs for Gr, *h*-BN, and MoS₂, respectively. For Gr, the dataset comprises two types of structures (see SI Figure S2). The first type includes monolayer periodic Gr in a $5 \times 6 \times 1$ supercell. We sampled 100 structures from *ab initio* molecular dynamics (AIMD) simulations at temperatures ranging from 100 K to 1500 K, and generated additional 50 structures by applying random perturbations ranging from -3% to 3%. The second type consists of randomly hydrogenated, non-periodic structures across six configurations: non-periodic squares with 60 and 54 carbon atoms, non-periodic rectangles with 60 and 46 carbon atoms, and armchair and zigzag nanoribbons containing 54 and 69 atoms, respectively. Hydrogenation was introduced to enable the applicability of the NEP at open boundaries, with hydrogen coverages ranging from 0% to 100% in 10% increments. To efficiently sample the reference configurations, we employed MD simulations using the MACE-MP-0 model [86] over a temperature range of 100 K to 1500 K. For each configuration, 55 structures were generated, 5 for each hydrogenation level, resulting in a total of 480 structures. Single-point DFT calculations were subsequently performed to obtain the energies, atomic forces, and virials required for constructing the reference datasets for MLPs training. Among these, 384 structures (80%) were used for training, and the remaining 96 (20%) for testing. A similar approach was adopted for preparing the reference datasets of *h*-BN and MoS₂, except that edge structures were not considered for MoS₂. More details are provided in SI Section S2.

C. MD simulation details

MD simulations for mechanical property evaluation were performed using the LAMMPS package [81]. To determine the bulk modulus of graphite system, simulations were conducted with periodic boundary conditions in all three spatial directions, and the equations of motion were integrated with a time step of 1 fs. The system temperature was set at 300 K using a Nosé–Hoover thermostat with a relaxation time of 0.25 ps. For simulations under hydrostatic pressure, a Nosé–Hoover barostat [109, 110] with a damping constant of 1.0 ps was employed. To construct the P – V curves, simulations were conducted in the NPT ensemble at 300 K under varying target pressures. Each system was equilibrated for 100 ps, followed by a 100 ps production run during which the average system volume was recorded. This procedure was repeated for hydrostatic pressures ranging from 0 to 14 GPa to estimate the bulk modulus.

Uniaxial tensile simulations were performed by incrementally deforming the simulation box along either the armchair or zigzag direction to evaluate the Young’s modulus and Poisson’s ratio of the graphite system, while maintaining zero stress along the transverse direction using the NPT ensemble at 300 K. The strain was applied in 0.02% increments with a time step of 1 fs. In each increment, the system was uniaxially stretched at a constant strain rate of 1×10^{-4} /ps to reach the target strain, followed by a 0.5 ns relaxation stage in the NPT ensemble to ensure stress equilibration in the transverse direction. Strain and stress were recorded and statistically averaged over the final 0.2 ns of each relaxation stage.

D. Structural optimization

All structural optimizations for vdW heterostructures were performed using the conjugate gradient (CG) [111] and FIRE algorithms [112] in LAMMPS. To achieve the most optimized structures, we performed 10 iterations of

the three algorithms: CG with box relaxation [113], CG with fixed box, FIRE with fixed box. In each loop, the relaxation procedure is terminated when the forces acting on each degree of freedom reduce below 1×10^{-6} eV/Å or the optimizing steps reach 100,000.

ACKNOWLEDGMENTS

W.O. acknowledges support from the National Natural Science Foundation of China (Nos. 12472099 and U2441207) and the Fundamental Research Funds for the Central Universities (No. 600460100). P.Y. is supported by the Israel Academy of Sciences and Humanities & Council for Higher Education Excellence Fellowship Program for International Postdoctoral Researchers. Computations were conducted at the Supercomputing Center of Wuhan University, the National Supercomputer TianHe-1(A) Center in Tianjin and Computing Center in Xi’an.

Conflict of Interest The authors have no conflicts to disclose.

Data availability Complete input and output files for the NEP training of monolayer Gr, h -BN and MoS₂ are freely available at https://github.com/ouyang-laboratory/nep_data. In LAMMPS, documentation for ILP is available at https://docs.lammps.org/pair_ilp_graphene_hbn.html and https://docs.lammps.org/pair_ilp_tmd.html, respectively. The NEP interface to LAMMPS is available at https://github.com/brucefan1983/NEP_CPU. In GPUMD, documentation for the hybrid NEP+ILP potential is available at https://gpumd.org/dev/potentials/nep_ilp.html. The hybrid NEP+ILP potential is currently available in the master branch of GPUMD (<https://github.com/brucefan1983/GPUMD>) and will be released later with GPUMD-v4.0.

-
- [1] K. Liu and J. Wu, Mechanical properties of two-dimensional materials and heterostructures, *Journal of Materials Research* **31**, 832 (2016).
 - [2] W. Ouyang, O. Hod, and M. Urbakh, Parity-dependent Moiré superlattices in graphene/ h -BN heterostructures: A route to mechanomutable metamaterials, *Physical Review Letters* **126**, 216101 (2021).
 - [3] Y. Liu, Z.-Y. Ong, J. Wu, Y. Zhao, K. Watanabe, T. Taniguchi, D. Chi, G. Zhang, J. T. Thong, C.-W. Qiu, and K. Hippalgaonkar, Thermal conductance of the 2D MoS₂/ h -BN and graphene/ h -BN interfaces, *Scientific reports* **7**, 43886 (2017).
 - [4] X. Wu and Q. Han, Phonon thermal transport across multilayer graphene/hexagonal boron nitride van der Waals heterostructures, *ACS Applied Materials & Interfaces* **13**, 32564 (2021).
 - [5] S. E. Kim, F. Mujid, A. Rai, F. Eriksson, J. Suh, P. Poddar, A. Ray, C. Park, E. Fransson, Y. Zhong, D. A. Muller, P. Erhart, D. G. Cahill, and J. Park, Extremely anisotropic van der Waals thermal conductors, *Nature* **597**, 660 (2021).
 - [6] L. Zhang, Y. Zhong, X. Li, J.-H. Park, Q. Song, L. Li, L. Guo, J. Kong, and G. Chen, Effect of twist angle on interfacial thermal transport in two-dimensional bilayers, *Nano Letters* **23**, 7790 (2023).
 - [7] Y. Cheng, Z. Fan, T. Zhang, M. Nomura, S. Volz, G. Zhu, B. Li, and S. Xiong, Magic angle in thermal conductivity of twisted bilayer graphene, *Materials Today Physics* **35**, 101093 (2023).
 - [8] A. K. Geim and I. V. Grigorieva, Van der Waals het-

- erostructures, *Nature* **499**, 419 (2013).
- [9] S. Kezilebieke, M. N. Huda, V. Vaño, M. Aapro, S. C. Ganguli, O. J. Silveira, S. Głodzik, A. S. Foster, T. Ojanen, and P. Liljeroth, Topological superconductivity in a van der Waals heterostructure, *Nature* **588**, 424 (2020).
- [10] H. Wang, S. Wang, S. Zhang, M. Zhu, W. Ouyang, and Q. Li, Deducing the internal interfaces of twisted multilayer graphene via Moiré-regulated surface conductivity, *National Science Review* **10**, nwad175 (2023).
- [11] J. Liu, X. Yang, H. Fang, W. Yan, W. Ouyang, and Z. Liu, In situ twistrionics: A new platform based on superlubricity, *Advanced Materials* (2023), 2305072, 10.1002/adma.202305072.
- [12] E. Koren, I. Leven, E. Lörtscher, A. Knoll, O. Hod, and U. Duerig, Coherent commensurate electronic states at the interface between misoriented graphene layers, *Nature Nanotechnology* **11**, 752 (2016).
- [13] S. Zhang, Q. Xu, Y. Hou, A. Song, Y. Ma, L. Gao, M. Zhu, T. Ma, L. Liu, X.-Q. Feng, and Q. Li, Domino-like stacking order switching in twisted monolayer-multilayer graphene, *Nature Materials* **21**, 621 (2022).
- [14] O. Hod, E. Meyer, Q. Zheng, and M. Urbakh, Structural superlubricity and ultralow friction across the length scales, *Nature* **563**, 485 (2018).
- [15] P. Ying, X. Gao, D. Berman, O. Hod, and M. Urbakh, Scaling-up of structural superlubricity: Challenges and opportunities, *Advanced Functional Materials* (2025), 2423024, 10.1002/adfm.202423024.
- [16] Y. Song, D. Mandelli, O. Hod, M. Urbakh, M. Ma, and Q. Zheng, Robust microscale superlubricity in graphite/hexagonal boron nitride layered heterojunctions, *Nature materials* **17**, 894 (2018).
- [17] P. Ying, O. Hod, and M. Urbakh, Superlubric graphullerene, *Nano Letters* **24**, 10599 (2024).
- [18] Z. Zhang, Y. Chen, P. Shen, J. Chen, S. Wang, B. Wang, S. Ma, B. Lyu, X. Zhou, S. Lou, Z. Wu, Y. Xie, C. Zhang, L. Wang, K. Xu, H. Li, G. Wang, K. Watanabe, T. Taniguchi, D. Qian, J. Jia, Q. Liang, X. Wang, W. Yang, G. Zhang, C. Jin, W. Ouyang, and Z. Shi, Homochiral carbon nanotube van der Waals crystals, *Science* **387**, 1310 (2025).
- [19] Y. Yao, Y. Song, B. Wu, S. Scherb, S. Huang, A. Hinaut, T. Glatzel, E. Meyer, Z. Liu, and W. Ouyang, Unraveling the interfacial properties of twisted single-crystal Au(111)/MoS₂ heterostructures: A pathway to robust superlubricity, *Advanced Science* (2025), 2415884, 10.1002/advs.202415884.
- [20] S. Zhang, Q. Yao, L. Chen, C. Jiang, T. Ma, H. Wang, X.-Q. Feng, and Q. Li, Dual-scale stick-slip friction on graphene/h-BN Moiré superlattice structure, *Physical Review Letters* **128**, 226101 (2022).
- [21] D. W. Brenner, O. A. Shenderova, J. A. Harrison, S. J. Stuart, B. Ni, and S. B. Sinnott, A second-generation reactive empirical bond order (REBO) potential energy expression for hydrocarbons, *Journal of Physics: Condensed Matter* **14**, 783 (2002).
- [22] S. J. Stuart, A. B. Tutein, and J. A. Harrison, A reactive potential for hydrocarbons with intermolecular interactions, *The Journal of Chemical Physics* **112**, 6472 (2000).
- [23] J. Tersoff, Empirical interatomic potential for carbon, with applications to amorphous carbon, *Physical Review Letters* **61**, 2879 (1988).
- [24] L. Lindsay and D. A. Broido, Optimized Tersoff and Brenner empirical potential parameters for lattice dynamics and phonon thermal transport in carbon nanotubes and graphene, *Physical Review B* **81**, 205441 (2010).
- [25] F. H. Stillinger and T. A. Weber, Computer simulation of local order in condensed phases of silicon, *Physical Review B* **31**, 5262 (1985).
- [26] J. Jiang and Y. Zhou, in *Handbook of Stillinger-Weber Potential Parameters for Two-Dimensional Atomic Crystals*, edited by J.-W. Jiang and Y.-P. Zhou (IntechOpen, Rijeka, 2017) Chap. 1.
- [27] J. Los and A. Fasolino, Intrinsic long-range bond-order potential for carbon: Performance in Monte Carlo simulations of graphitization, *Physical Review B* **68**, 024107 (2003).
- [28] J. H. Los, L. M. Ghiringhelli, E. J. Meijer, and A. Fasolino, Improved long-range reactive bond-order potential for carbon. I. Construction, *Physical Review B—Condensed Matter and Materials Physics* **72**, 214102 (2005).
- [29] M. Reguzzoni, A. Fasolino, E. Molinari, and M. C. Righi, Potential energy surface for graphene on graphene: Ab initio derivation, analytical description, and microscopic interpretation, *Physical Review B—Condensed Matter and Materials Physics* **86**, 245434 (2012).
- [30] A. N. Kolmogorov and V. H. Crespi, Registry-dependent interlayer potential for graphitic systems, *Physical Review B* **71**, 235415 (2005).
- [31] I. V. Lebedeva, A. A. Knizhnik, A. M. Popov, Y. E. Lozovik, and B. V. Potapkin, Interlayer interaction and relative vibrations of bilayer graphene, *Physical Chemistry Chemical Physics* **13**, 5687 (2011).
- [32] A. N. Kolmogorov and V. H. Crespi, Smoothest bearings: Interlayer sliding in multiwalled carbon nanotubes, *Physical Review Letters* **85**, 4727 (2000).
- [33] I. Leven, I. Azuri, L. Kronik, and O. Hod, Inter-layer potential for hexagonal boron nitride, *The Journal of Chemical Physics* **140**, 104106 (2014).
- [34] I. Leven, T. Maaravi, I. Azuri, L. Kronik, and O. Hod, Interlayer potential for graphene/h-BN heterostructures, *Journal of Chemical Theory and Computation* **12**, 2896 (2016).
- [35] T. Maaravi, I. Leven, I. Azuri, L. Kronik, and O. Hod, Interlayer potential for homogeneous graphene and hexagonal boron nitride systems: Reparametrization for many-body dispersion effects, *The Journal of Physical Chemistry C* **121**, 22826 (2017).
- [36] W. Ouyang, D. Mandelli, M. Urbakh, and O. Hod, Nanoserpents: Graphene nanoribbon motion on two-dimensional hexagonal materials, *Nano Letters* **18**, 6009 (2018).
- [37] W. Ouyang, R. Sofer, X. Gao, J. Hermann, A. Tkatchenko, L. Kronik, M. Urbakh, and O. Hod, Anisotropic interlayer force field for transition metal dichalcogenides: The case of molybdenum disulfide, *Journal of Chemical Theory and Computation* **17**, 7237 (2021).
- [38] W. Jiang, R. Sofer, X. Gao, A. Tkatchenko, L. Kronik, W. Ouyang, M. Urbakh, and O. Hod, Anisotropic interlayer force field for group-VI transition metal dichalcogenides, *The Journal of Physical Chemistry A* **127**, 9820 (2023).

- [39] W. Jiang, R. Sofer, X. Gao, L. Kronik, O. Hod, M. Urbakh, and W. Ouyang, Anisotropic interlayer force field for interfaces of graphene and h-BN with transition metal dichalcogenides, *The Journal of Physical Chemistry C* **129**, 1417 (2025).
- [40] A. Tkatchenko and M. Scheffler, Accurate molecular van der Waals interactions from ground-state electron density and free-atom reference data, *Physical review letters* **102**, 073005 (2009).
- [41] M. Vizner Stern, Y. Waschitz, W. Cao, I. Nevo, K. Watanabe, T. Taniguchi, E. Sela, M. Urbakh, O. Hod, and M. Ben Shalom, Interfacial ferroelectricity by van der Waals sliding, *Science* **372**, 1462 (2021).
- [42] D. Mandelli, W. Ouyang, M. Urbakh, and O. Hod, The princess and the nanoscale pea: Long-range penetration of surface distortions into layered materials stacks, *ACS Nano* **13**, 7603 (2019).
- [43] W. Ouyang, I. Azuri, D. Mandelli, A. Tkatchenko, L. Kronik, M. Urbakh, and O. Hod, Mechanical and tribological properties of layered materials under high pressure: Assessing the importance of many-body dispersion effects, *Journal of Chemical Theory and Computation* **16**, 666 (2020).
- [44] W. Ouyang, O. Hod, and M. Urbakh, Registry-dependent peeling of layered material interfaces: The case of graphene nanoribbons on hexagonal boron nitride, *ACS Applied Materials & Interfaces* **13**, 43533 (2021).
- [45] B. Wu, Y. Pan, Y. Yao, W. Ouyang, and Z. Liu, Facet-governed frictional behavior in graphene/h-BN heteronanotubes, *Extreme Mechanics Letters* **68**, 102144 (2024).
- [46] K. Huang, H. Qin, S. Zhang, Q. Li, W. Ouyang, and Y. Liu, The origin of Moiré-level stick-slip behavior on graphene/h-BN heterostructures, *Advanced Functional Materials* **32**, 2204209 (2022).
- [47] W. Yan, W. Ouyang, and Z. Liu, Origin of frictional scaling law in circular twist layered interfaces: Simulations and theory, *Journal of the Mechanics and Physics of Solids* **170**, 105114 (2023).
- [48] W. Yan, X. Gao, W. Ouyang, Z. Liu, O. Hod, and M. Urbakh, Shape-dependent friction scaling laws in twisted layered material interfaces, *Journal of the Mechanics and Physics of Solids* **185**, 105555 (2024).
- [49] W. Ouyang, H. Qin, M. Urbakh, and O. Hod, Controllable thermal conductivity in twisted homogeneous interfaces of graphene and hexagonal boron nitride, *Nano Letters* **20**, 7513 (2020).
- [50] W. Jiang, T. Liang, J. Xu, and W. Ouyang, Twist-dependent anisotropic thermal conductivity in homogeneous MoS₂ stacks, *International Journal of Heat and Mass Transfer* **217**, 124662 (2023).
- [51] W. Jiang, T. Liang, H. Bu, J. Xu, and W. Ouyang, Moiré-driven interfacial thermal transport in twisted transition metal dichalcogenides, (2025), arXiv:2503.09141.
- [52] B. Lyu, J. Chen, S. Wang, S. Lou, P. Shen, J. Xie, L. Qiu, I. Mitchell, C. Li, C. Hu, *et al.*, Graphene nanoribbons grown in hBN stacks for high-performance electronics, *Nature* **628**, 758 (2024).
- [53] B. Lyu, J. Chen, S. Lou, C. Li, L. Qiu, W. Ouyang, J. Xie, I. Mitchell, T. Wu, A. Deng, C. Hu, X. Zhou, P. Shen, S. Ma, Z. Wu, K. Watanabe, T. Taniguchi, X. Wang, Q. Liang, J. Jia, M. Urbakh, O. Hod, F. Ding, S. Wang, and Z. Shi, Catalytic growth of ultralong graphene nanoribbons on insulating substrates, *Advanced Materials* **34**, 2200956 (2022).
- [54] Z. Feng, Y. Yao, J. Liu, B. Wu, Z. Liu, and W. Ouyang, Registry-dependent potential for interfaces of water with graphene, *The Journal of Physical Chemistry C* **127**, 8704 (2023).
- [55] Z. Feng, Z. Lei, Y. Yao, J. Liu, B. Wu, and W. Ouyang, Anisotropic interfacial force field for interfaces of water with hexagonal boron nitride, *Langmuir* **39**, 18198 (2023).
- [56] Q. Liang, W. Jiang, Y. Liu, and W. Ouyang, Anisotropic interlayer force field for two-dimensional hydrogenated carbon materials and their heterostructures, *The Journal of Physical Chemistry C* **127**, 18641 (2023).
- [57] Y. Yao, B. Wu, Z. Liu, and W. Ouyang, Semi-anisotropic interfacial potential for interfaces between metal and 2D carbon allotrope, *The Journal of Physical Chemistry C* **128**, 6836 (2024).
- [58] W. Ouyang, O. Hod, and R. Guerra, Registry-dependent potential for interfaces of gold with graphitic systems, *Journal of Chemical Theory and Computation* **17**, 7215 (2021).
- [59] C. Qian, B. McLean, D. Hedman, and F. Ding, A comprehensive assessment of empirical potentials for carbon materials, *APL Materials* **9**, 061102 (2021).
- [60] P. Ying, H. Dong, T. Liang, Z. Fan, Z. Zhong, and J. Zhang, Atomistic insights into the mechanical anisotropy and fragility of monolayer fullerene networks using quantum mechanical calculations and machine-learning molecular dynamics simulations, *Extreme Mechanics Letters* **58**, 101929 (2023).
- [61] J. Behler and M. Parrinello, Generalized neural-network representation of high-dimensional potential-energy surfaces, *Physical Review Letters* **98**, 146401 (2007).
- [62] P. Friederich, F. Häse, J. Proppe, and A. Aspuru-Guzik, Machine-learned potentials for next-generation matter simulations, *Nature Materials* **20**, 750 (2021).
- [63] A. P. Bartók, M. C. Payne, R. Kondor, and G. Csányi, Gaussian approximation potentials: The accuracy of quantum mechanics, without the electrons, *Phys. Rev. Lett.* **104**, 136403 (2010).
- [64] A. V. Shapeev, Moment tensor potentials: A class of systematically improvable interatomic potentials, *Multiscale Modeling & Simulation* **14**, 1153 (2016).
- [65] L. Zhang, J. Han, H. Wang, R. Car, and W. E, Deep potential molecular dynamics: A scalable model with the accuracy of quantum mechanics, *Physical Review Letters* **120**, 143001 (2018).
- [66] R. Drautz, Atomic cluster expansion for accurate and transferable interatomic potentials, *Phys. Rev. B* **99**, 014104 (2019).
- [67] Z. Fan, Z. Zeng, C. Zhang, Y. Wang, K. Song, H. Dong, Y. Chen, and T. Ala-Nissila, Neuroevolution machine learning potentials: Combining high accuracy and low cost in atomistic simulations and application to heat transport, *Physical Review B* **104**, 104309 (2021).
- [68] I. Batatia, D. P. Kovacs, G. Simm, C. Ortner, and G. Csányi, MACE: Higher order equivariant message passing neural networks for fast and accurate force fields, *Advances in neural information processing systems* **35**, 11423 (2022).
- [69] S. Batzner, A. Musaelian, L. Sun, M. Geiger, J. P. Mailoa, M. Kornbluth, N. Molinari, T. E. Smidt, and

- B. Kozinsky, E(3)-equivariant graph neural networks for data-efficient and accurate interatomic potentials, *Nature Communications* **13**, 2453 (2022).
- [70] B. Cheng, Cartesian atomic cluster expansion for machine learning interatomic potentials, *npj Computational Materials* **10**, 157 (2024).
- [71] J. Wang, Y. Wang, H. Zhang, Z. Yang, Z. Liang, J. Shi, H.-T. Wang, D. Xing, and J. Sun, E(n)-Equivariant cartesian tensor message passing interatomic potential, *Nature Communications* **15**, 7607 (2024).
- [72] P. Rowe, G. Csányi, D. Alfè, and A. Michaelides, Development of a machine learning potential for graphene, *Physical Review B* **97**, 054303 (2018).
- [73] P. Ying, A. Natan, O. Hod, and M. Urbakh, Effect of interlayer bonding on superlubric sliding of graphene contacts: A machine-learning potential study, *ACS Nano* **18**, 10133 (2024).
- [74] T. Liang, K. Xu, P. Ying, W. Jiang, M. Han, X. Wu, W. Ouyang, Y. Yao, X. Zeng, Z. Ye, Z. Fan, and J. Xu, Probing the ideal limit of interfacial thermal conductance in two-dimensional van der Waals heterostructures, (2025), [arXiv:2502.13601](https://arxiv.org/abs/2502.13601).
- [75] Y. Gao, F. Deng, R. He, and Z. Zhong, Spontaneous curvature in two-dimensional van der Waals heterostructures, *Nature Communications* **16**, 717 (2025).
- [76] P. Ying and Z. Fan, Combining the D3 dispersion correction with the neuroevolution machine-learned potential, *Journal of Physics: Condensed Matter* **36**, 125901 (2024).
- [77] M. Wen and E. B. Tadmor, Hybrid neural network potential for multilayer graphene, *Physical Review B* **100**, 195419 (2019).
- [78] V. L. Deringer, M. A. Caro, and G. Csányi, A general-purpose machine-learning force field for bulk and nanostructured phosphorus, *Nature Communications* **11**, 5461 (2020).
- [79] Z. Fan, Improving the accuracy of the neuroevolution machine learning potential for multi-component systems, *Journal of Physics: Condensed Matter* **34**, 125902 (2022).
- [80] Z. Fan, Y. Wang, P. Ying, K. Song, J. Wang, Y. Wang, Z. Zeng, K. Xu, E. Lindgren, J. M. Rahm, A. J. Gabourie, J. Liu, H. Dong, J. Wu, Y. Chen, Z. Zhong, J. Sun, P. Erhart, Y. Su, and T. Ala-Nissila, GPUMD: A package for constructing accurate machine-learned potentials and performing highly efficient atomistic simulations, *The Journal of Chemical Physics* **157**, 114801 (2022).
- [81] A. P. Thompson, H. M. Aktulga, R. Berger, D. S. Bolinteanu, W. M. Brown, P. S. Crozier, P. J. In't Veld, A. Kohlmeyer, S. G. Moore, T. D. Nguyen, *et al.*, LAMMPS—a flexible simulation tool for particle-based materials modeling at the atomic, meso, and continuum scales, *Computer physics communications* **271**, 108171 (2022).
- [82] Z. Fan, W. Chen, V. Vierimaa, and A. Harju, Efficient molecular dynamics simulations with many-body potentials on graphics processing units, *Computer Physics Communications* **218**, 10 (2017).
- [83] J. R. Gissinger, I. Nikiforov, Y. Afshar, B. Waters, M.-k. Choi, D. S. Karls, A. Stukowski, W. Im, H. Heinz, A. Kohlmeyer, and E. B. Tadmor, Type label framework for bonded force fields in LAMMPS, *The Journal of Physical Chemistry B* **128**, 3282 (2024).
- [84] P. Gao, X. Duan, J. Guo, J. Wang, Z. Song, L. Cui, X. Meng, X. Liu, W. Zhang, M. Ma, G. Li, D. Chen, H. Fu, W. Xue, W. Liu, and G. Yang, in *Proceedings of the International Conference for High Performance Computing, Networking, Storage and Analysis*, SC '21 (Association for Computing Machinery, New York, NY, USA, 2021).
- [85] S. Grimme, J. Antony, S. Ehrlich, and H. Krieg, A consistent and accurate ab initio parametrization of density functional dispersion correction (DFT-D) for the 94 elements H-Pu, *The Journal of chemical physics* **132**, 154104 (2010).
- [86] I. Batatia, P. Benner, Y. Chiang, A. M. Elena, D. P. Kovács, J. Riebesell, X. R. Advincula, M. Asta, M. Avaylon, W. J. Baldwin, F. Berger, N. Bernstein, A. Bhowmik, S. M. Blau, V. Cărare, J. P. Darby, S. De, F. Della Pia, V. L. Deringer, R. Elijošius, Z. El-Machachi, F. Falcioni, E. Fako, A. C. Ferrari, A. Genreith-Schriever, J. George, R. E. A. Goodall, C. P. Grey, P. Grigorev, S. Han, W. Handley, H. H. Heenen, K. Hermansson, C. Holm, J. Jaafar, S. Hofmann, K. S. Jakob, H. Jung, V. Kapil, A. D. Kaplan, N. Karimitari, J. R. Kermode, N. Kroupa, J. Kullgren, M. C. Kuner, D. Kuryla, G. Liepuoniute, J. T. Margraf, I.-B. Magdău, A. Michaelides, J. H. Moore, A. A. Naik, S. P. Niblett, S. W. Norwood, N. O'Neill, C. Ortner, K. A. Persson, K. Reuter, A. S. Rosen, L. L. Schaaf, C. Schran, B. X. Shi, E. Sivonxay, T. K. Stenczel, V. Svahn, C. Sutton, T. D. Swinburne, J. Tilly, C. van der Oord, E. Varga-Umbrich, T. Vegge, M. Vondrák, Y. Wang, W. C. Witt, F. Zills, and G. Csányi, A foundation model for atomistic materials chemistry, (2024), [arXiv:2401.00096](https://arxiv.org/abs/2401.00096).
- [87] L. Wirtz and A. Rubio, The phonon dispersion of graphite revisited, *Solid State Communications* **131**, 141 (2004).
- [88] R. W. Lynch and H. G. Drickamer, Effect of high pressure on the lattice parameters of diamond, graphite, and hexagonal boron nitride, *The Journal of Chemical Physics* **44**, 181 (1966).
- [89] Y. X. Zhao and I. L. Spain, X-ray diffraction data for graphite to 20 GPa, *Phys. Rev. B* **40**, 993 (1989).
- [90] M. Hanfland, H. Beister, and K. Syassen, Graphite under pressure: Equation of state and first-order Raman modes, *Phys. Rev. B* **39**, 12598 (1989).
- [91] S. Clark, K.-J. Jeon, J. Chen, and C.-S. Yoo, Few-layer graphene under high pressure: Raman and X-ray diffraction studies, *Solid State Communications* **154**, 15 (2013).
- [92] J. Hermann and A. Tkatchenko, Density functional model for van der Waals interactions: Unifying many-body atomic approaches with nonlocal functionals, *Physical Review Letters* **124**, 146401 (2020).
- [93] J. P. Perdew, K. Burke, and M. Ernzerhof, Generalized gradient approximation made simple, *Physical Review Letters* **77**, 3865 (1996).
- [94] K. Song, R. Zhao, J. Liu, Y. Wang, E. Lindgren, Y. Wang, S. Chen, K. Xu, T. Liang, P. Ying, N. Xu, Z. Zhao, J. Shi, J. Wang, S. Lyu, Z. Zeng, S. Liang, H. Dong, L. Sun, Y. Chen, Z. Zhang, W. Guo, P. Qian, J. Sun, P. Erhart, T. Ala-Nissila, Y. Su, and Z. Fan, General-purpose machine-learned potential for 16 elemental metals and their alloys, *Nature Communications* **15**, 10208 (2024).

- [95] T. Schaul, T. Glasmachers, and J. Schmidhuber, in *Proceedings of the 13th Annual Conference on Genetic and Evolutionary Computation* (ACM, Dublin Ireland, 2011) pp. 845–852.
- [96] F. D. Murnaghan, The compressibility of media under extreme pressures, *Proceedings of the National Academy of Sciences* **30**, 244 (1944).
- [97] F. Birch, Finite elastic strain of cubic crystals, *Phys. Rev.* **71**, 809 (1947).
- [98] F. Birch, Elasticity and constitution of the Earth's interior, *Journal of Geophysical Research (1896-1977)* **57**, 227 (1952).
- [99] P. Vinet, J. Ferrante, J. R. Smith, and J. H. Rose, A universal equation of state for solids, *Journal of Physics C: Solid State Physics* **19**, L467 (1986).
- [100] P. Vinet, J. R. Smith, J. Ferrante, and J. H. Rose, Temperature effects on the universal equation of state of solids, *Phys. Rev. B* **35**, 1945 (1987).
- [101] C. Lee, X. Wei, J. W. Kysar, and J. Hone, Measurement of the elastic properties and intrinsic strength of monolayer graphene, *Science* **321**, 385 (2008).
- [102] O. L. Blakslee, D. G. Proctor, E. J. Seldin, G. B. Spence, and T. Weng, Elastic constants of compression-annealed pyrolytic graphite, *Journal of Applied Physics* **41**, 3373 (1970).
- [103] X. Huang, L. Chen, S. Tang, C. Jiang, C. Chen, H. Wang, Z.-X. Shen, H. Wang, and Y.-T. Cui, Imaging dual-Moiré lattices in twisted bilayer graphene aligned on hexagonal boron nitride using microwave impedance microscopy, *Nano Letters* **21**, 4292 (2021).
- [104] I. Leven, R. Guerra, A. Vanossi, E. Tosatti, and O. Hod, Multiwalled nanotube faceting unravelled, *Nature nanotechnology* **11**, 1082 (2016).
- [105] R. Niu, Z. Li, X. Han, Z. Qu, Q. Liu, Z. Wang, C. Han, C. Wang, Y. Wu, C. Yang, M. Lv, K. Yang, K. Watanabe, T. Taniguchi, K. Liu, J. Mao, W. Shi, R. Che, W. Zhou, J. Xue, M. Wu, B. Peng, Z. V. Han, Z. Gan, and J. Lu, Ferroelectricity with concomitant Coulomb screening in van der Waals heterostructures, *Nature Nanotechnology* **20**, 346 (2025).
- [106] G. Kresse and J. Furthmüller, Efficient iterative schemes for *ab initio* total-energy calculations using a plane-wave basis set, *Physical Review B* **54**, 11169 (1996).
- [107] G. Kresse and D. Joubert, From ultrasoft pseudopotentials to the projector augmented-wave method, *Phys. Rev. B* **59**, 1758 (1999).
- [108] P. E. Blöchl, Projector augmented-wave method, *Physical Review B* **50**, 17953 (1994).
- [109] W. Shinoda, M. Shiga, and M. Mikami, Rapid estimation of elastic constants by molecular dynamics simulation under constant stress, *Phys. Rev. B* **69**, 134103 (2004).
- [110] T. C. O'Connor, J. Andzelm, and M. O. Robbins, AIREBO-M: A reactive model for hydrocarbons at extreme pressures, *The Journal of Chemical Physics* **142**, 024903 (2015).
- [111] A. Schwartz and E. Polak, Family of projected descent methods for optimization problems with simple bounds, *Journal of Optimization Theory and Applications* **92**, 1 (1997).
- [112] E. Bitzek, P. Koskinen, F. Gähler, M. Moseler, and P. Gumbsch, Structural relaxation made simple, *Physical Review Letters* **97**, 170201 (2006).
- [113] M. Parrinello and A. Rahman, Polymorphic transitions in single crystals: A new molecular dynamics method, *Journal of Applied Physics* **52**, 7182 (1981).